# Nonequilibrium phonon transport across nanoscale interfaces

Georgios Varnavides,[1,2,3] Adam S. Jermyn,[4,5] Polina Anikeeva,[1,2,*] and Prineha Narang[3,†]

[1]*Department of Materials Science and Engineering, Massachusetts Institute of Technology, Cambridge, Massachusetts 02139, USA*
[2]*Research Laboratory of Electronics, Massachusetts Institute of Technology, Cambridge, Massachusetts 02139, USA*
[3]*John A. Paulson School of Engineering and Applied Sciences, Harvard University, Cambridge, Massachusetts 02138, USA*
[4]*Kavli Institute for Theoretical Physics, University of California at Santa Barbara, Santa Barbara, California 93106, USA*
[5]*Institute of Astronomy, University of Cambridge, Madingley Road, Cambridge CB3 0HA, England, United Kingdom*

(Received 8 November 2018; revised manuscript received 19 August 2019; published 3 September 2019)

Despite the ubiquity of applications of heat transport across nanoscale interfaces, including integrated circuits, thermoelectrics, and nanotheranostics, an accurate description of phonon transport in these systems remains elusive. Here we present a theoretical and computational framework to describe phonon transport with position, momentum, and scattering event resolution. We apply this framework to a single-material nanoparticle for which this multidimensional resolution offers insight into the physical origin of phonon thermalization and the length-scale dependent anisotropy of driven phonon distributions. We extend the formalism to handle interfaces and investigate the specific case of semicoherent materials interfaces by computing the coupling between phonons and interfacial strain resulting from a periodic array of misfit dislocations. We calculate the thermal interface conductance within the technologically relevant Si-Ge heterostructures and obtain $G = 173.2\ \mathrm{MW\,m^{-2}\,K^{-1}}$, in good agreement with previous experimental and theoretical work. Finally we comment on future applications of our framework including coherent and driven phonon effects in nanoscale materials, which are increasingly accessible via ultrafast, terahertz, and near-field spectroscopies.

DOI: 10.1103/PhysRevB.100.115402

## I. INTRODUCTION

Understanding phonon-mediated heat transfer at the nanoscale is essential to the design and optimization of heat management for a variety of engineering systems including thermoelectrics [1], nanoelectronics [2,3], catalytic cells [4], and nanotheranostics [5]. Advances in ultrafast probes of coherent dynamics have revealed nonequilibrium regimes of phonon transport, necessitating a new theoretical framework describing these effects [6–9].

Despite its success, the phenomenological heat conduction equation is known to break down at both short lengthscales and short timescales [10–13] as well as in low-dimensional materials [14]. In such instances it is necessary to use the more general phonon Boltzmann transport equation (pBTE) [15]. This formalism recovers the phenomenological result in the hydrodynamic limit [16] and provides the most general description of semiclassical phonon transport by tracking the evolution of probability distributions in full phase space, resolving both spatial and momentum degrees of freedom.

Shortly after it was proposed, linearized solutions of the pBTE enabled predictions of lattice thermal conductivity of crystalline insulators using the relaxation-time approximation (RTA) [17], which assumes all perturbations return to equilibrium with the same timescale [18]. Under the RTA the collision term in the pBTE is diagonal in both position and momentum space, making it possible to solve the pBTE with both time and spatial resolution [19,20]. Recent computational methods have enabled the linearized pBTE to be solved exactly, beyond the RTA, using materials parameters determined from first principles via variational [21–23], iterative [24,25], and direct approaches [26–28]. However, each of these theoretical studies solved the time- and space-independent form of the pBTE, i.e., at a steady state assuming a spatially homogeneous structure, reducing the problem dimensionality to the three-momentum degrees of freedom.

An accurate picture of heat transport addressing finite-size effects and transport across interfaces, however, must include the spatial degrees of freedom of the nanoscale geometry [29]. This paper aims to fill this void in theoretical transport methods by incorporating all momentum degrees of freedom into a spatially resolved pBTE solver, building on our previous work in excited carrier dynamics [30–32].

The starting point for describing steady-state phonon transport is the time-independent pBTE given by

$$\boldsymbol{v}_{\boldsymbol{q},s} \cdot \nabla n(\boldsymbol{q}, s, \boldsymbol{r}) = G_0(\boldsymbol{q}, s, \boldsymbol{r}) + \Gamma_{\boldsymbol{q},s}[n], \tag{1}$$

where $\boldsymbol{q}$ and $s$ are the phonon momentum and polarization, respectively, $\boldsymbol{r}$ is position, $n(\boldsymbol{q}, s, \boldsymbol{r})$ is the phonon distribution function, and $\boldsymbol{v}_{\boldsymbol{q},s}$ is the phonon group velocity. The term on the left reflects phonon drift with velocity $\boldsymbol{v}_{\boldsymbol{q},s}$, while the terms on the right account for phonon generation $[G_0(\boldsymbol{q}, s, \boldsymbol{r})]$ and collisions $(\Gamma_{\boldsymbol{q},s}[n])$.

We linearize Eq. (1) and find [30,33]

$$\boldsymbol{v}_{\mu} \cdot \nabla \psi(\mu, \boldsymbol{r}) = G_0(\mu, \boldsymbol{r}) + \sum_{\mu'} A_{\mu\mu'} \psi(\mu', \boldsymbol{r}), \tag{2}$$

*anikeeva@mit.edu
†prineha@seas.harvard.edu

 ©2019 American Physical Society

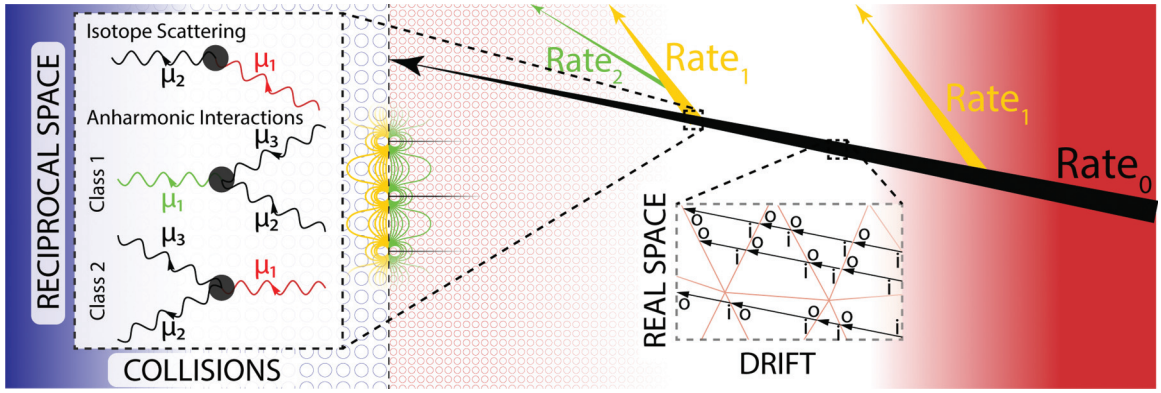


FIG. 1. Schematic description of the recursive formulation and computational implementation of the pBTE. Phonons are injected at a constant rate, $G_0$. We capture their drift through the real-space structure by solving Eq. (5a) using the finite element method with linear elements (Appendix D). The mixing matrix, consisting of three-phonon interactions and isotopic scattering (Appendix B), is then applied to the unscattered distribution $\psi_0$ according to Eq. (5b), giving the rate at which phonons are generated due to the first scattering event, $G_1$. Green and yellow dilatational contours sketch the interface model described in Eq. (8).

where $\mu$ is a phonon label encapsulating both $\boldsymbol{q}$ and $s$ and

$$\psi_\mu(\boldsymbol{r}) = \frac{n(\mu,\boldsymbol{r}) - \bar{n}(\mu,\boldsymbol{r})}{\bar{n}(\mu,\boldsymbol{r})[\bar{n}(\mu,\boldsymbol{r})+1]} \tag{3}$$

is the normalized deviation from the equilibrium Bose-Einstein distribution $\bar{n}(\mu,\boldsymbol{r})$. The scattering matrix $A_{\mu\mu'}$ specifies the rate at which phonons scatter from state $\mu$ into state $\mu'$ and is given by the first-order series expansion of $\Gamma_\mu[n]$ around the equilibrium. For notational convenience we omit the position dependence of $\psi_\mu$ hereinafter.

The scattering matrix can be split into diagonal terms, representing decay, and off-diagonal terms, constituting the mixing matrix (Appendices A and B):

$$A_{\mu\mu'} = \tau_\mu^{-1}\delta_{\mu\mu'} + M_{\mu\mu'}. \tag{4a}$$

Likewise, the phonon distribution $\psi$ may be expanded as

$$\psi = \psi^{(0)} + \psi^{(1)} + \psi^{(2)} + \cdots, \tag{4b}$$

where $\psi^{(m)}$ collects contributions at $m$th order in $M$, encoding the population of carriers which are connected to the source $G_0$ by $m$ scattering events. Substitution of Eqs. (4a) and (4b) into Eq. (2) returns the linearized recurrence relations

$$\left(\tau_\mu^{-1} + v_\mu \cdot \nabla\right)\psi_\mu^{(m)} = G_m(\mu) \tag{5a}$$

and

$$G_{m+1}(\mu) = \sum_{\mu'} M_{\mu\mu'}\psi_{\mu'}^{(m)}. \tag{5b}$$

These relations, indexed by scattering event $m$, illustrate our method of treating collisions purely in reciprocal space, and drift purely in real space, thus precluding any quantum effects in drift. Each iteration in the algorithm represents a physical scattering event, the significance of which can be traced back to the thermalization of carriers, illustrated schematically in Fig. 1.

Temperature gradients inside a material are modeled by a constant source of phonons, $G_0$. These phonons drift in real space on a dense finite element mesh, as modeled by the solution to Eq. (5a), before scattering against the background phonon distribution. This produces phonons at a different constant rate $G_1$, given by Eq. (5b), which is taken as the injection rate of phonons that have scattered once. The procedure is then repeated until the convergence of Eq. (4b), which is aided by the positive-semidefinite nature of the scattering matrix $A$ (Appendices A and B).

## II. SINGLE MATERIAL VALIDATION

To demonstrate the utility of our spatially resolved formalism we apply it to examine phonon transport in a silicon nanoparticle with a diameter of 200 nm, and a constant injection of thermal phonons at the origin (Appendix D). The steady-state distribution converges after only a few scattering events [Fig. 2(a)]. This is because the nanoscale dimensions of the nanoparticle favor quasiballistic rather than diffusive transport [quantified by Fig. 4(a) and further discussed below].

Despite operating in steady state, our framework enables the examination of individual scattering events, thus offering microscopic insight into transient processes inaccessible to the heat conduction equation. We find that the scattering event resolved distributions qualitatively match the transient behavior obtained by treating the constant source term as an initial population instead [Fig. 2(b)]. In some ways scattering events are a more physical descriptor of thermalization than time, which is effectively the former convolved with carriers' mean free paths. This highlights the physical origin of carrier thermalization as a direct consequence of scattering in the material, and suggests that our formalism may offer insights into transient phenomena.

Next, we analyze the accumulated distribution of carriers reaching the surface as a function of scattering events. In position space, the distribution of carriers is anisotropic with "hot" and "cold" regions [Fig. 3(a)]. This is a consequence of two phenomena. First, due to their quasiballistic behavior many carriers reach the surface without scattering. Second, the carriers exhibit anisotropic group velocities [Fig. 3(c)] and thus preferentially reach the surface at latitudes corresponding

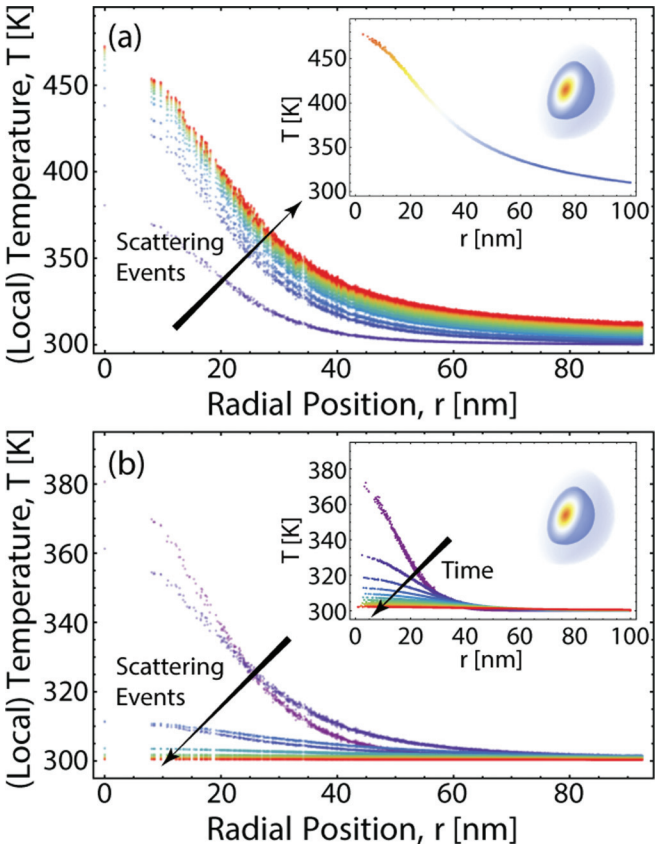


FIG. 2. Spatially resolved thermal transport in a silicon nanoparticle. (a) Accumulated radial temperature profile at steady state, after 15 scattering events. The diminishing differences in the temperature profile distribution with increasing scattering events indicate the rapid convergence. Inset: Solution to Fourier's equation with similar boundary conditions. (b) Individual contributions to the temperature profile at order $m$. Inset: Transient solution to Fourier's equation with similar initial conditions.

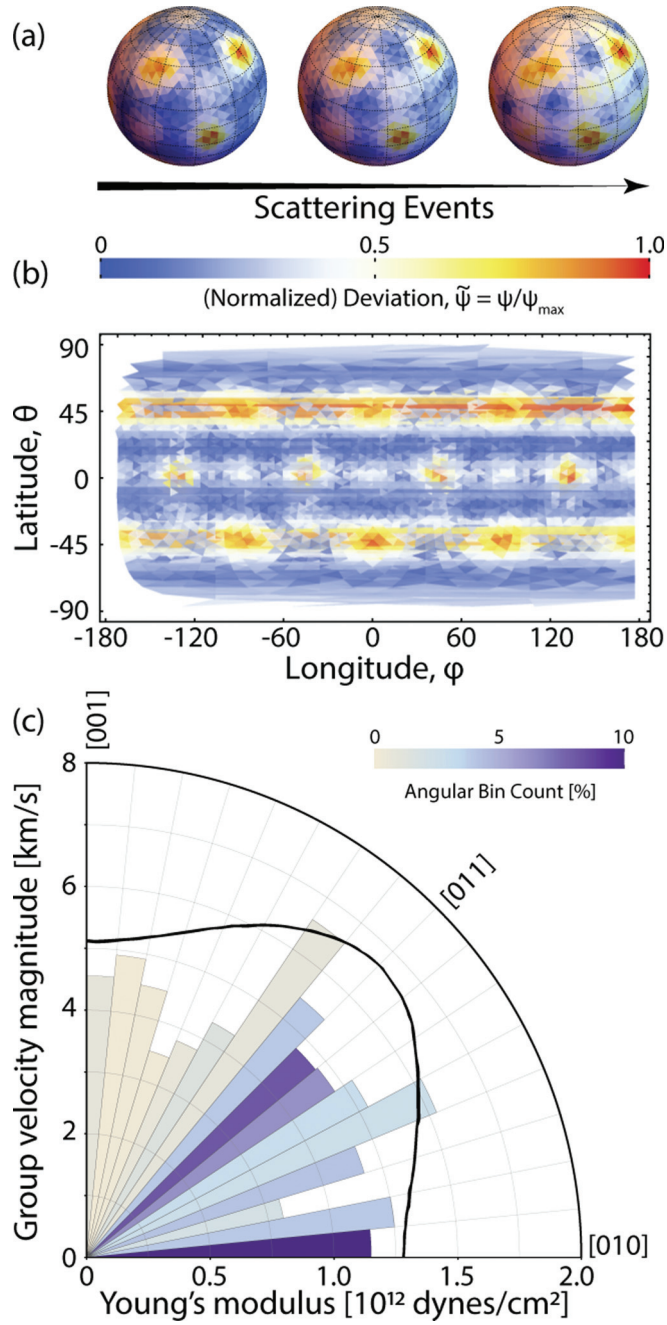


FIG. 3. Anisotropic surface carrier distribution. (a) Accumulated surface distribution of carriers as a function of scattering events, highlighting the real-space anisotropy at earlier scattering events. (b) Angular projection of the surface distribution at the first scattering event, illustrating accumulation at lines of constant latitude. (c) Directional dependence of phonon velocity magnitudes in the (100) plane. The black line highlights the analogy with Young's modulus, reproduced from [34].

to densely sampled directions in the group velocity distribution [Fig. 3(b)]. Considering phonons in the long-wavelength limit, this can be traced to the anisotropy of the elastic stiffness tensor for cubic materials [34]. Subsequent scattering events work to isotropize the distribution [Fig. 3(a)], as anticipated from symmetry considerations in cubic materials.

## III. INTERFACE TRANSPORT

The spatial and scattering event resolution of our formalism presents an opportunity to investigate interface transport outside the Landauer formalism [35]. When heat is conducted through interfaces the local temperature exhibits a sharp discontinuity, giving rise to thermal interface resistance (TIR), which was first described by Kapitza in 1941 [36] and has since been studied rigorously for a variety of materials [37].

The earliest models to describe TIR, the acoustic mismatch model (AMM) [38] and the diffuse mismatch model (DMM) [39], make use of the Landauer formalism attributing scattering to a mismatch of vibrational properties across the interface. While the influence of atomic roughness is especially significant at higher temperatures, both models underestimate TIR at moderate cryogenic temperatures and above, attributed to the omission of inelastic scattering [40,41]. At higher temperatures, anharmonic interactions become important to TIR, and despite the development of refined models to include full dispersion relations [40], and address anharmonicity [41], the corrections come at additional computational costs. Recently,

an alternative approach using nonequilibrium molecular dynamics (NEMD) has been demonstrated, capable of capturing TIR in the classical limit [42–45].

We propose an alternative formalism in which we specify an interface Hamiltonian and compute transition probabilities using Fermi's "golden rule." Within our recursive framework, surface fluxes are expressed as

$$S_\mu = (\boldsymbol{v}_\mu \cdot \hat{\boldsymbol{a}})\psi_\mu, \tag{6}$$

where $\hat{\boldsymbol{a}}$ is the surface normal. This can be extended for a heterostructure between materials $i$ and $j$ as

$$S_\mu^{i,m+1} = T_{\mu\mu'}^{i\to j} \cdot S_{\mu'}^{j',m} + R_{\mu\mu'}^{i\to j} \cdot S_{\mu'}^{i',m}, \tag{7}$$

and similarly for $S_\mu^{j,m+1}$. Here $T^{i\to j}$ and $R^{i\to j}$ represent transmission and reflectance matrices, $m$ indexes scattering events, and the prime superscript specifies only those nodes shared at the interface [46]. This splits the phonon flux into material $i$ into a component being backscattered at the interface and a component being transmitted at the interface from the incoming flux from material $j$.

### Strain mismatch model

We illustrate our approach via a simple example of a structure-specific interface Hamiltonian, describing semicoherent interfaces such as a silicon-germanium heterostructure [47]. Such semicoherent interfaces are characterized by the spontaneous formation of linear arrays of misfit (edge) dislocations [47], characterized by a periodic dilatational strain field along the interface. This external strain couples to phonons [48], leading to inelastic scattering of the latter at the interface. We now sketch the derivation of the interface Hamiltonian. In the presence of a strain field, the potential energy of a crystal is determined by the total atomic displacement, $u_{\text{total}} = u_{\text{ph}} + u_{\text{strain}}$ [48]. This can be represented as a Taylor series around equilibrium in increasing powers of displacement, with the cubic term giving the lowest-order anharmonic contribution [33]. Expanding, we obtain four interaction categories: (1) three-phonon interactions ($u_{\text{ph}}^3$), (2) two-phonon interactions with strain ($u_{\text{strain}}u_{\text{ph}}^2$), (3) one-phonon interactions with strain ($u_{\text{strain}}^2 u_{\text{ph}}$), and (4) vacuum interactions ($u_{\text{strain}}^3$).

The first category captures regular three-phonon interactions, which are found in the bulk independent of strain. The fourth category leads to a constant shift in energy and so can be omitted. Single-phonon interactions with strain do not conserve energy to first order, and can be shown to cancel out exactly at higher orders [48]. We thus focus on two-phonon interactions with the strain field, described by the perturbation Hamiltonian:

$$H' = \frac{\hbar}{4\rho\Omega} c_2(\mu_1, \mu_2) \prod_{i=1}^{2} \left(a_{\mu_i}^\dagger + a_{\mu_{-i}}\right), \tag{8}$$

where $\rho$ is the material density, $\Omega$ is the unit-cell volume, $a^\dagger(a)$ are the phonon creation (annihilation) operators, and $c_2$ is the phonon-strain coupling coefficient (Appendix C). We thus arrive at a conceptual picture of TIR: a phonon in state $\mu$ in material $i$ interacts with the Fourier component of the interfacial strain, scattering into a phonon in state $\mu'$ in material $i$ or $j$, transferring the excess momentum to the strain field [48]. The model, termed the strain mismatch model (SMM), is shown schematically in Fig. 1. We use expressions from linear elasticity for the dilatational strain field due to misfit dislocations (Appendix C) [49].

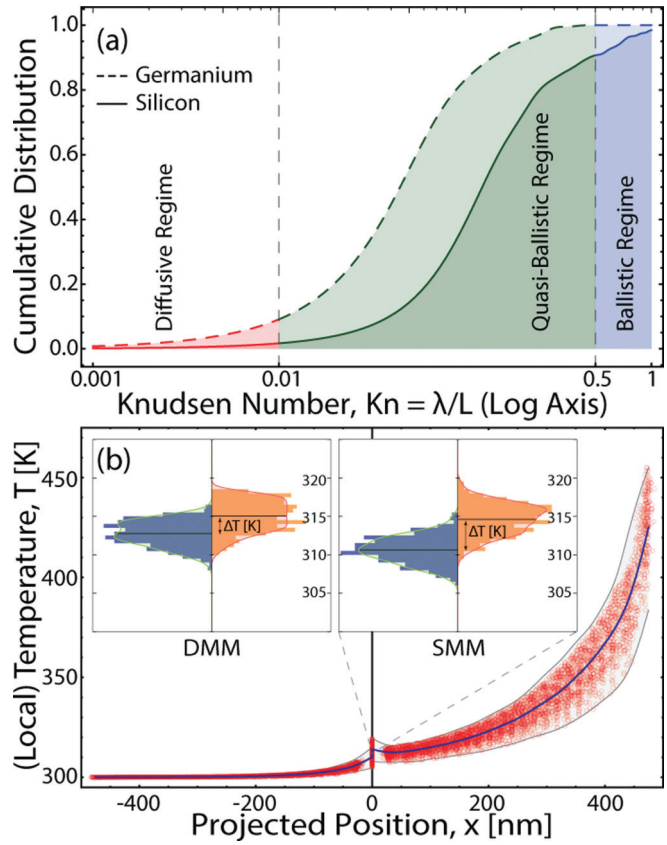


FIG. 4. Thermal interface conductance. (a) Cumulative distribution of carrier Knudsen numbers, showing that less than 10% of carriers are purely "diffusive." (b) Steady-state local temperature profile across a Si-Ge heterostructure using the SMM. Red circles show the x-projected position of local temperature, with the smooth blue line showing the x-binned mean local temperature. Inset: Comparison of the local temperatures at each side of the interface for both DMM and SMM.

Table I shows the thermal conductance calculated with our formalism for both the DMM and SMM approaches, as well as from other models. We also compare these with inferred thermal conductances from Si/Ge superlattice experiments [53]. All calculations are performed on a heterojunction between 500-nm cubes of Si and Ge at 300 K. Such nanoscale dimensions favor quasiballistic transport. This is quantified in Fig. 4(a) by the nondimensional Knudsen number of carriers, highlighting the nondiffusive character of the system and explaining the nonlinear temperature profile away from the interface.

The local temperature discontinuity across the interface is recovered in position space using both the DMM and the SMM [Fig. 4(b)]. The computed thermal conductance using the DMM is in good agreement with the theoretical value using the Landauer formalism [50], albeit both

TABLE I. Interface thermal conductance comparison with prior theoretical work and Si/Ge superlattice experiments.

| | Theoretical work | | | | Experimental superlattice period | | | |
|---|---|---|---|---|---|---|---|---|
| | DMM[a] | DMM[b] | NEMD | SMM[b] | 9.0 nm | 14.0 nm | 15.0 nm | 27.5 nm |
| $G$(MW m$^{-2}$ K$^{-1}$) | 417.5 [50] | 392.5 | 315.9 [50] | 173.2 | 711 [51] | 414 [51] | 276 [52] | 159 [52] |

[a]Landauer formalism.
[b]This paper.

overestimate compared to NEMD and larger superlattice period experiments [52]. Table I and Fig. 4(b) summarize the additional interface scattering correctly captured by the SMM, which achieves higher accuracy on larger superlattice period experiments. This can be attributed to inelastic scattering at the interface, and is expected to be even more pronounced at higher temperatures.

## IV. SUMMARY

In this paper, we establish a theoretical and computational framework for semiclassical transport that describes all six degrees of freedom of the BTE at steady state. We have applied our recursive formalism to phonon transport, with *ab initio* calculated scattering matrices, utilizing the multidimensional resolution to investigate the physical origins of phonon thermalization and anisotropic phonon distributions. We have extended the framework to compute phonon surface fluxes and investigated heat transport across interfaces. Our perturbative formalism was validated against a semicoherent interface within a Si-Ge heterostructure—a ubiquitous materials system in nanoelectronics. The model confirms that nonintrinsic phonon scattering near the interface plays a dominant role in TIR, and provides a pathway for generalization to other structure-specific interfaces. Our paper may advance thermal transport engineering at nanostructured materials interfaces including those found in thermoelectrics, energy storage, and nanotheranostic agents. By resolving individual scattering events, our formalism could also provide insight into transient behavior of phonons and capture nonequilibrium phenomena such as coherent phonon effects in all-optical characterization of band structures of semiconductor heterostructures.

## ACKNOWLEDGMENTS

The authors thank Prof. W. Craig Carter and Nicholas Rivera of the Massachusetts Institute of Technology for fruitful discussions. G.V. and P.N. acknowledge funding from the Defense Advanced Research Projects Agency Defense Sciences Office Driven and Nonequilibrium Quantum Systems program and an ONR grant on High-$T_c$ Superconductivity at Oxide-Chalcogenide Interfaces (Grant No. N00014-18-1-2691). A.S.J. thanks the United Kingdom Marshall Commission for financial support. A.S.J. acknowledges support by the Gordon and Betty Moore Fundation (Grant No. GBMF7392) and the National Science Foundation (Grant No. PHY-1748958).

## APPENDIX A: RECURSIVE SOLUTION DERIVATION

We derive the recursive solution to a general ballistic transport problem with linear collision and a source term. This is governed by the differential equation

$$\sum_j \left(\frac{D}{Dt}\right)_{ij} \phi_j = S_i^{(0)} - \sum_j C_{ij}\phi_j, \tag{A1}$$

where $S^{(0)}$ is the initial source term, $C$ is the collision matrix, and $\phi$ is the vector density of states the evolution of which we would like to track. The differential operator $D/Dt$ is defined as

$$\left(\frac{D}{Dt}\right) = \left(\frac{\partial}{\partial t} + \sum_k v_{ik}\nabla_k\right)\delta_{ij}, \tag{A2}$$

where $v$ is the ballistic velocity operator and $\nabla$ is the nabla operator. In steady state, $\partial/\partial t \to 0$, and Eq. (A1) reduces to

$$\sum_k v_{ik}\nabla_k\phi_i = S_i^{(0)} - \sum_j C_{ij}\phi_j. \tag{A3}$$

This can be rewritten in the form

$$\sum_j \left(\delta_{ij}\sum_k v_{ik}\nabla_k + C_{ij}\right)\phi_j = S_i^{(0)}, \tag{A4}$$

which highlights that, for a given discretization of space, the solution $\phi$ may be obtained via a matrix inversion. The matrix to be inverted, however, exists over the joint space of spatial and state dimensions, so instead we proceed iteratively. We first split $C$ into diagonal and off-diagonal terms:

$$C_{ij} = \tau_i^{-1}\delta_{ij} + M_{ij}, \tag{A5}$$

where $\tau_i$ is the lifetime of the carrier in state $i$. We may thereby express Eq. (A4) as

$$\sum_j \left(\delta_{ij}\sum_k v_{ik}\nabla_k + \delta_{ij}\tau_i^{-1}\right)\phi_j = S_i^{(0)} + \sum_j M_{ij}\phi_j, \tag{A6}$$

where the operator which acts on $\phi$ on the left-hand side is diagonal in state space, and the operator which acts on it on the right-hand side is diagonal in position space.

Let $G_i$ be the Green's function which inverts this operator. Our iteration scheme then amounts to the following:

$$\phi_i^{(n)} = G_i\left(S_i^{(n)}\right), \tag{A7a}$$

$$S_i^{(n+1)} = -\sum_j M_{ij}\phi_j^{(n)}, \tag{A7b}$$

where $\phi_i^{(n)}$ depends on the $n$th power of $G$, defined via

$$\phi_i = \sum_{n=0}^{\infty} \phi_i^{(n)}. \tag{A8}$$

Equations (A7a) and (A7b) may be written in a form similar to the Jacobi iterative method:

$$\phi^{(n)} = -GM\phi^{(n-1)}, \tag{A9}$$

where all summation indices have been dropped for clarity. The iterative scheme converges if and only if the spectral radius of $GM$ is less than unity. This is not guaranteed *a priori*, so the scheme could fail. To remedy this, we switch to a *weighted* Jacobi scheme:

$$\phi^{(n)} = -\omega GM\phi^{(n-1)} + (1-\omega)\phi^{(n-1)}, \tag{A10a}$$

$$\phi^{(0)} = \omega GS^{(0)}, \tag{A10b}$$

where $\omega \in (0, 1)$ is the weight parameter, chosen so that the spectral radius of $\omega GM$ is less than unity. This converges as long as the matrix $(G^{-1} - M)$ is diagonally dominant.

Because the joint position-state space over which $GM$ is defined is extremely large we cannot explicitly construct this operator and hence cannot directly use its spectral radius to motivate a choice of $\omega$. However, the Green's function acting on a spatially homogeneous system reduces to $\tau_i\delta_{ij}$, so we may use the operator $\tau M$ to estimate the spectral radius of $GM$. We show below that the collision matrix $C$ is strictly diagonally dominant, motivating this scheme at least in the spatially homogeneous case.

A number of our observations rely on the exact scattering history, which is only strictly equal to $\phi^{(n)}$ for a choice of $\omega = 1$. To address this, we reconstruct the scattering history *a posteriori*. Let the iteration matrix $Q = -GM$ and note that Eq. (A10a) can be written as

$$\phi^{(n)} = \sum_{j=0}^{n} (\omega Q)^j (1-\omega)^{n-j} \binom{n}{j} \phi^{(0)}. \tag{A11}$$

Since $Q$ is the operator which scatters and propagates carriers, we can define the population of carriers following $k$ scattering events, $\psi_k$, as those that arrive via $k$ applications of $Q$:

$$\psi_k = \sum_{n=k}^{\infty} \omega^k (1-\omega)^{n-k} \binom{n}{k} Q^k \phi^{(0)}. \tag{A12}$$

In order to calculate $\psi_k$, we need access to $Q^k\phi^{(0)}$. This can be accomplished by separating Eq. (A11),

$$\phi^{(n)} = \sum_j Z_{nj} Q^j \phi^{(0)}, \tag{A13a}$$

to a purely combinatorial component,

$$Z_{nj} = \omega^j (1-\omega)^{n-j} \binom{n}{j}, \tag{A13b}$$

to finally obtain

$$Q^k\phi^{(0)} = \sum_l Z_{jl}^{-1} \phi^{(n)}. \tag{A14}$$

With Eq. (A14) it is possible to compute $\psi_k$ and thus reconstruct the full scattering history as a postprocessing step. This is guaranteed to be possible, since $Z$ is nonsingular.

## APPENDIX B: ANHARMONIC SCATTERING

We consider two types of anharmonic scattering processes inside bulk materials, namely, three-phonon scattering and phonon-isotope scattering. The intrinsic three-phonon scattering can be further separated into "coalescence processes" (+) and "decay processes" (−) the rates of which are given by [21,54]

$$P^{\pm}_{\boldsymbol{qs},\boldsymbol{q'}s',\boldsymbol{q''}s''} = 2\pi\bar{n}_{\boldsymbol{qs}}\left(\bar{n}_{\boldsymbol{q'}s'} + \frac{1}{2} \mp \frac{1}{2}\right)(\bar{n}_{\boldsymbol{q''}s''} + 1) \times |V_3(-\boldsymbol{qs}, \mp\boldsymbol{q'}s', \boldsymbol{q''}s'')|^2 \delta(\omega_{\boldsymbol{qs}} \pm \omega_{\boldsymbol{q'}s'} - \omega_{\boldsymbol{q''}s''}). \tag{B1}$$

$V_3(\boldsymbol{qs}, \boldsymbol{q'}s', \boldsymbol{q''}s'')$ is the anharmonic coupling given by

$$V_3(\boldsymbol{qs}, \boldsymbol{q'}s', \boldsymbol{q''}s'') = \left(\frac{\hbar}{8N\omega_{\boldsymbol{qs}}\omega_{\boldsymbol{q'}s'}\omega_{\boldsymbol{q''}s''}}\right)^{1/2} \sum_{bb'b''}\sum_{\alpha\beta\gamma} \tilde{\Psi}_{\alpha\beta\gamma} \times (\boldsymbol{q}b, \boldsymbol{q'}b', \boldsymbol{q''}b'')(m_b m_{b'} m_{b''})^{-1/2} \times e_\alpha(b|\boldsymbol{qs}) e_\beta(b'|\boldsymbol{q'}s') e_\gamma(b''|\boldsymbol{q''}s''). \tag{B2}$$

$\boldsymbol{e}(b|\boldsymbol{qs})$ is the eigenvector of the $b$th atom in mode $\boldsymbol{qs}$, $m$ are atomic masses, $N$ is the number of $\boldsymbol{q}$ points, and greek letters denote Cartesian directions. $\tilde{\Psi}(\boldsymbol{q}b, \boldsymbol{q'}b', \boldsymbol{q''}b'')$ is the Fourier-transformed third-order interatomic force constants tensor given by

$$\tilde{\Psi}(\boldsymbol{q}b, \boldsymbol{q'}b', \boldsymbol{q''}b'') = \sum_{l'l''} \Psi(0b, l'b', l''b'') e^{i\boldsymbol{q'}l'} e^{i\boldsymbol{q''}l''}, \tag{B3}$$

where $l$ is a supercell index, and all other symbols are as previously defined.

Similarly, the rate for a phonon-isotope event is [21]

$$P^{\text{isot}}_{\boldsymbol{qs},\boldsymbol{q'}s'} = \frac{\pi}{2N}\left(\bar{n}_{\boldsymbol{qs}}\bar{n}_{\boldsymbol{q'}s'} + \frac{\bar{n}_{\boldsymbol{qs}} + \bar{n}_{\boldsymbol{q'}s'}}{2}\right)\omega_{\boldsymbol{qs}}\omega_{\boldsymbol{q'}s'} \times \sum_b g_b \left|\sum_\alpha e_\alpha(b|\boldsymbol{qs})^* \cdot e_\alpha(b|\boldsymbol{q'}s')\right|^2 \delta(\omega_{\boldsymbol{qs}} - \omega_{\boldsymbol{q'}s'}), \tag{B4}$$

where

$$g_b = \frac{(m_b - \langle m_b\rangle)^2}{\langle m_b\rangle^2} \tag{B5}$$

is the mass average of atom $b$.

Combining Eqs. (B3) and (B4), the total anharmonic scattering matrix inside bulk materials is given by [21,33]

$$A_{\mu,\mu'} = \left[\sum_{\mu'',\mu'''}\left(P^+_{\mu,\mu''',\mu''} + \frac{P^+_{\mu'',\mu''',\mu}}{2}\right) + \sum_{\mu''} P^{\text{isot}}_{\mu,\mu''}\right]\delta_{\mu,\mu'} - \sum_{\mu''}(P^-_{\mu,\mu'',\mu'} - P^-_{\mu,\mu',\mu''} + P^-_{\mu',\mu'',\mu}) + P^{\text{isot}}_{\mu,\mu'}, \tag{B6}$$

where we used the compact mode index $\mu$, as before.

It can be shown that the scattering matrix is positive semidefinite [21], a stricter condition than our required diagonally dominant condition. The iterative scheme is thus guaranteed to converge for appropriate choices of weight $\omega$ as long as the spatial degrees of freedom do not amplify the spectral radius of the system. This is unlikely to emerge, as spatially varying systems lose carriers more readily than infinite homogeneous ones, though the possibility remains that our scheme could become ill conditioned.

## APPENDIX C: INTERFACIAL STRAIN COUPLING

We start with Eq. (8), i.e., the perturbation Hamiltonian describing phonon-strain coupling, and derive the scattering rates following Carruthers [48,55]:

$$H' = \frac{\hbar}{4\rho\Omega} c_2(\mu_1, \mu_2) \prod_{i=1}^{2} \left(a^\dagger_{\mu_i} + a_{\mu_{-i}}\right). \tag{C1}$$

The process involves two phonons (as evidenced by the product of two pairs of creation/annihilation operators), coupling to the external strain field via

$$c_2(\boldsymbol{q}s, \boldsymbol{q}'s') = \sum_{bb'b''} \sum_{\alpha\beta\gamma} \tilde{\Psi}_{\alpha\beta\gamma}(\boldsymbol{q}b, \boldsymbol{q}'b', (\boldsymbol{q}'-\boldsymbol{q})b'') \times \frac{e_\alpha(b|\boldsymbol{q}s)}{\sqrt{\omega_{\boldsymbol{q}s} m_b}} \frac{e_\beta(b'|\boldsymbol{q}'s')}{\sqrt{\omega_{\boldsymbol{q}'s'} m_{b'}}} v_\gamma(\boldsymbol{q}'-\boldsymbol{q}), \tag{C2}$$

where the excess momentum is evaluated at the Fourier-transformed external strain field $\boldsymbol{v}(\boldsymbol{q}'-\boldsymbol{q})$.

Using Eqs. (C1) and (C2), the scattering rate is therefore given by

$$P^{\text{strain}}_{\boldsymbol{q}s,\boldsymbol{q}'s'} = \frac{\pi}{8\rho^2\Omega^2} \left(\bar{n}_{\boldsymbol{q}s}\bar{n}_{\boldsymbol{q}'s'} + \frac{\bar{n}_{\boldsymbol{q}s} + \bar{n}_{\boldsymbol{q}'s'}}{2}\right) \times |c_2(\boldsymbol{q}s, \boldsymbol{q}'s')|^2 \delta(\omega_{\boldsymbol{q}s} - \omega_{\boldsymbol{q}'s'}). \tag{C3}$$

We note that $\hbar s$ cancel out, making the result classical.

We now turn to deriving the external strain for the specific case of a semicoherent interface. In particular, we look at the dilatation caused by misfit dislocations. The displacement fields for a single edge dislocation are readily provided by linear elasticity as [49]

$$\begin{aligned} u_x &= \frac{b}{2\pi}\left[\theta + \frac{\sin(2\theta)}{4(1-\nu)}\right], \\ u_y &= -\frac{b}{2\pi}\left[\frac{(1-2\nu)}{2(1-\nu)}\log\left(\frac{r_0}{r}\right) + \frac{\cos(2\theta)}{4(1-\nu)}\right], \\ u_z &= 0, \end{aligned} \tag{C4}$$

where $b$ is the magnitude of the dislocation Burger vector, $\nu$ is the material's Poisson ratio, $r_0$ is the dislocation core radius, and $r$ and $\theta$ are polar coordinates. The dilatation of Eq. (C4) for the usual approximation of $r_0 \approx b$ is

$$\begin{aligned} \Delta(r) &= \nabla \cdot \{u_x, u_y, u_z\} = -\frac{b}{2\pi}\left[\frac{1-2\nu}{2(1-\nu)}\frac{\sin\theta}{r}\right], \\ \Delta(x,y) &= -\frac{b}{2\pi}\left[\frac{1-2\nu}{2(1-\nu)}\frac{y}{x^2+y^2}\right]. \end{aligned} \tag{C5}$$

Working under the assumption of linear elasticity, we can express the additive dilatation of an infinite array of edge dislocations with a period $d$ as

$$\begin{aligned} \Delta^\infty(x,y) &= -\frac{b}{2\pi}\left[\frac{1-2\nu}{2(1-\nu)}\right]\sum_{n=-\infty}^{\infty}\frac{y}{(x-nd)^2+y^2} \\ &= -\frac{b}{2\pi}\left[\frac{1-2\nu}{2(1-\nu)}\right]\frac{\sinh(2\pi y/d)}{\cosh(2\pi y/d)-\cos(2\pi x/d)}, \end{aligned} \tag{C6}$$

where we note that the result is (naturally) periodic along the interface. The dilatational field is plotted in Fig. 1. We can take the Fourier transform of Eq. (C6) by the change of variables $\alpha = 2\pi x/d$, $\beta = 2\pi y/d$, $k_x = q_x d/2\pi$, and $k_y = q_y d/2\pi$ to give

$$\Delta^\infty(q) = -\frac{b}{\Omega^{2/3}}\left[\frac{1-2\nu}{(1-\nu)}\right]\frac{iq_y}{\left(q_x^2+q_y^2\right)}, \tag{C7}$$

where the $\Omega^{2/3}$ factor was accumulated as a consequence of integrating along the interface. We can supplement Eq. (C7) with an additional factor of $\Delta(q_z)$ resulting from integrating out of plane, to obtain [55]

$$\boldsymbol{v}(\boldsymbol{q}) = \frac{b}{\Omega^{2/3}}\left[\frac{1-2\nu}{(1-\nu)}\right]\frac{q_y}{\left(q_x^4+2q_x^2q_y^2+q_y^4\right)}\Delta(q_z)\boldsymbol{q}. \tag{C8}$$

We note the natural result that $\boldsymbol{v}(\boldsymbol{q})$ is parallel to $\boldsymbol{q}$ since the field's rotation, $R = \nabla \times \{u_x, u_y, u_z\}$, is zero.

Substituting Eqs. (C8) and (C2) into Eq. (C3), we can obtain the scattering rate for a given phonon in state $\mu$ to couple with the static strain field and scatter into a phonon in state $\mu'$. Finally, we make the assumption that interatomic force constants are evaluated on the material the incoming phonon state $\mu$ is coming from. We compute the reflection/transmission tensors by normalizing these rates to the sum of all final states (energy conservation), by noting that if phonon states $\mu$ and $\mu'$ are taken from the same material we are calculating a reflection probability, whereas if the initial and final states are taken from different materials we are calculating a transmission probability.

## APPENDIX D: COMPUTATIONAL DETAILS

The recursive solution to the pBTE developed herein requires both material properties and real structure inputs, as well as the constant injection profile, $G_0$. We compute material properties, namely, the phonon group velocities and the third-order truncated scattering matrix, using first-principles calculations. The real-space structure is discretized on a finite element mesh with linear elements.

All first-principles calculations were performed using QUANTUM ESPRESSO [56,57], based on density functional perturbation theory. In particular, third-order interatomic force constants and anharmonic scattering rates were computed using the D3Q and THERMAL2 suite of codes [21,58–62]. For diamond (germanium) calculations we used a $6 \times 6 \times 6$ $\boldsymbol{k}$-point electronic Monkhorst-Pack mesh, with a norm-conserving pseudopotential with cutoff radius of 2.4 (2.6) a.u. The exchange-correlation functional used was under the local-density approximation, with a plane-wave

kinetic-energy cutoff of 34 (80) Ry and a charge density cutoff of 136 (320) Ry. Anharmonic forces were computed on a $6 \times 6 \times 6$ $\boldsymbol{q}$-point phonon grid. This was subsequently Fourier interpolated to a finer $10 \times 10 \times 10$ $\boldsymbol{q}$-point phonon mesh on which the full scattering matrix was computed, with a Gaussian smearing of $\sigma = 2.5(2)\text{cm}^{-1}$, at a temperature of 300 K.

The 200-nm-diameter silicon nanoparticle, used in validating the formalism, was discretized into 6364 vertices and 35781 linear tetrahedra, with an average volume of $116 \pm 38\,\text{nm}^3$. Similarly the silicon-germanium heterostructure, of dimensions $1000 \times 500 \times 500\,\text{nm}$, was discretized into 15474 vertices (729 of which were shared at the interface) and 76179 linear tetrahedra, with an average volume of $3281 \pm 142\text{nm}^3$.

In both calculations the constant source injections consisted of thermal phonons at temperatures higher than the equilibrium lattice. In particular, in the silicon nanoparticle we injected Bose-Einstein distributed phonons where the temperature, $T$, varied as a Gaussian with an amplitude of 125 K and a standard deviation of 15 nm (i.e., the phononic temperature at the nanoparticle origin was 425 K, decreasing to a constant value of 300 K roughly 50 nm away from the origin). Similarly, the constant source injection for the silicon-germanium heterostructure consisted of thermal phonons at 400 K at the right surface of the silicon. We use diffuse boundary conditions with the vacuum boundary; i.e., a phonon hitting the boundary scatters back to an energy-conserving state (enforced by the density of states) with 50% probability and it is lost otherwise.

In interpreting the nonequilibrium phonon distributions as a local temperature, we solve for the temperature at which the first moment of the distribution (energy density) agrees with that of a Bose-Einstein distribution:

$$\sum_{\mu} \hbar\omega_{\mu} n_{\mu} = \sum_{\mu} \hbar\omega_{\mu} \bar{n}_{\mu} = \sum_{\mu} \hbar\omega_{\mu} \left(e^{\frac{\hbar\omega_{\mu}}{k_B T}} - 1\right)^{-1}. \quad \text{(D1)}$$


[1] E. S. Toberer, A. Zevalkink, and G. J. Snyder, J. Materi. Chem. **21**, 15843 (2011).
[2] C. G. Van de Walle and R. M. Martin, Phys. Rev. B **34**, 5621 (1986).
[3] H. Adhikari, A. F. Marshall, C. E. D. Chidsey, and P. C. McIntyre, Nano Lett. **6**, 318 (2006).
[4] H. Robatjazi, H. Zhao, D. F. Swearer, N. J. Hogan, L. Zhou, A. Alabastri, M. J. McClain, P. Nordlander, and N. J. Halas, Nat. Commun. **8**, 27 (2017).
[5] L. Wang, M. C. Chuang, and J. A. Ho, Int. J. Nanomedicine **7**, 4679 (2012).
[6] K. Ishioka, A. Rustagi, A. Beyer, W. Stolz, K. Volz, U. Höfer, H. Petek, and C. J. Stanton, Appl. Phys. Lett. **111**, 062105 (2017).
[7] K. Ishioka, K. Brixius, A. Beyer, A. Rustagi, C. J. Stanton, W. Stolz, K. Volz, U. Höfer, and H. Petek, Appl. Phys. Lett. **108**, 051607 (2016).
[8] A. A. Maznev, J. A. Johnson, and K. A. Nelson, Phys. Rev. B **84**, 195206 (2011).
[9] K. Sokolowski-Tinten, C. Blome, J. Blums, A. Cavalleri, C. Dietrich, A. Tarasevitch, I. Uschmann, E. Förster, M. Kammler, M. H. von Hoegen, and D. von der Linde, Nature (London) **422**, 287 (2003).
[10] M. E. Siemens, Q. Li, R. Yang, K. A. Nelson, E. H. Anderson, M. M. Murnane, and H. C. Kapteyn, Nat. Mater. **9**, 26 (2009).
[11] A. J. Minnich, J. A. Johnson, A. J. Schmidt, K. Esfarjani, M. S. Dresselhaus, K. A. Nelson, and G. Chen, Phys. Rev. Lett. **107**, 095901 (2011).
[12] J. A. Johnson, A. A. Maznev, J. Cuffe, J. K. Eliason, A. J. Minnich, T. Kehoe, C. M. S. Torres, G. Chen, and K. A. Nelson, Phys. Rev. Lett. **110**, 025901 (2013).
[13] K. T. Regner, D. P. Sellan, Z. Su, C. H. Amon, A. J. McGaughey, and J. A. Malen, Nat. Commun. **4**, 1640 (2013).
[14] C. W. Chang, D. Okawa, H. Garcia, A. Majumdar, and A. Zettl, Phys. Rev. Lett. **101**, 075903 (2008).
[15] R. Peierls, Annalen der Physik **395**, 1055 (1929).
[16] J.-P. M. Péraud and N. G. Hadjiconstantinou, Phys. Rev. B **93**, 045424 (2016).
[17] P. Klemens, *Solid State Physics* (Elsevier, New York, 1958), pp. 1–98.
[18] J. Callaway, Phys. Rev. **113**, 1046 (1959).
[19] C. Hua and A. J. Minnich, Br. J. Appl. Phys. **117**, 175306 (2015).
[20] A. Majumdar, J. Heat Transfer **115**, 7 (1993).
[21] G. Fugallo, M. Lazzeri, L. Paulatto, and F. Mauri, Phys. Rev. B **88**, 045430 (2013).
[22] R. A. H. Hamilton and J. E. Parrott, Phys. Rev. **178**, 1284 (1969).
[23] G. P. Srivastava, J. Phys. C **9**, 3037 (1976).
[24] D. A. Broido, A. Ward, and N. Mingo, Phys. Rev. B **72**, 014308 (2005).
[25] M. Omini and A. Sparavigna, Phys. Rev. B **53**, 9064 (1996).
[26] R. A. Guyer and J. A. Krumhansl, Phys. Rev. **148**, 766 (1966).
[27] A. Cepellotti and N. Marzari, Phys. Rev. X **6**, 041013 (2016).
[28] L. Chaput, Phys. Rev. Lett. **110**, 265506 (2013).
[29] G. Romano and J. C. Grossman, J. Heat Transfer **137**, 071302 (2015).
[30] A. S. Jermyn, G. Tagliabue, H. A. Atwater, W. A. Goddard, III, P. Narang, and R. Sundararaman, Phys. Rev. Mater. **3**, 075201 (2019).
[31] A. M. Brown, R. Sundararaman, P. Narang, W. A. Goddard, III, and H. A. Atwater, Phys. Rev. B **94**, 075120 (2016).
[32] A. M. Brown, R. Sundararaman, P. Narang, A. M. Schwartzberg, W. A. Goddard, III, and H. A. Atwater, Phys. Rev. Lett. **118**, 087401 (2017).
[33] G. Srivastava, *The Physics of Phonons* (CRC, Boca Raton, FL, 1990).
[34] J. J. Wortman and R. A. Evans, Br. J. Appl. Phys. **36**, 153 (1965).
[35] S. Datta, *Electronic Transport in Mesoscopic Systems*, Cambridge Studies in Semiconductor Physics and Microelectronic Engineering (Cambridge University, Cambridge, England, 1995).
[36] P. L. Kapitza, Phys. Rev. **60**, 354 (1941).
[37] G. L. Pollack, Rev. Mod. Phys. **41**, 48 (1969).
[38] I. M. Khalatnikov, Zh. Eksp. Teor. Fiz. **22**, 687 (1952).

[39] E. T. Swartz and R. O. Pohl, Rev. Mod. Phys. **61**, 605 (1989).
[40] P. Reddy, K. Castelino, and A. Majumdar, Appl. Phys. Lett. **87**, 211908 (2005).
[41] R. S. Prasher and P. E. Phelan, J. Heat Transfer **123**, 105 (2001).
[42] K. Termentzidis, J. Parasuraman, C. D. Cruz, S. Merabia, D. Angelescu, F. Marty, T. Bourouina, X. Kleber, P. Chantrenne, and P. Basset, Nanoscale Res. Lett. **6**, 288 (2011).
[43] K. Termentzidis, T. Barreteau, Y. Ni, H. Huedro, A.-L. Delaye, X. Zianni, Y. Chalopin, P. Chantrenne, and S. Volz, J. Phys.: Conf. Series **395**, 012107 (2012).
[44] K. Gordiz and A. Henry, Br. J. Appl. Phys. **119**, 015101 (2016).
[45] K. Azizi, P. Hirvonen, Z. Fan, A. Harju, K. R. Elder, T. Ala-Nissila, and S. M. V. Allaei, Carbon **125**, 384 (2017).
[46] Interfaces include those with the vacuum as well as those between different materials.
[47] R. W. B. A. P. Sutton, *Interfaces in Crystalline Materials* (Oxford University, New York, 2007).
[48] P. Carruthers, Phys. Rev. **114**, 995 (1959).
[49] J. H. Weertman, *Dislocation Based Fracture Mechanics* (World Scientific, Singapore, 1996).
[50] E. S. Landry and A. J. H. McGaughey, Phys. Rev. B **80**, 165304 (2009).
[51] T. Borca-Tasciuc, W. Liu, J. Liu, T. Zeng, D. W. Song, C. D. Moore, G. Chen, K. L. Wang, M. S. Goorsky, T. Radetic, R. Gronsky, T. Koga, and M. S. Dresselhaus, Superlattices Microstruct. **28**, 199 (2000).
[52] S.-M. Lee, D. G. Cahill, and R. Venkatasubramanian, Appl. Phys. Lett. **70**, 2957 (1997).
[53] The experiments measure the cross-plane thermal conductivity across Si/Ge superlattices with varying period. From these we infer thermal conductance across the interface by assuming bulk phonon scattering is negligible.
[54] *Length-Scale Dependent Phonon Interactions*, edited by S. L. Shindé and G. P. Srivastava (Springer, New York, 2014).
[55] P. Carruthers, Rev. Mod. Phys. **33**, 92 (1961).
[56] P. Giannozzi, S. Baroni, N. Bonini, M. Calandra, R. Car, C. Cavazzoni, D. Ceresoli, G. L. Chiarotti, M. Cococcioni, I. Dabo, A. D. Corso, S. de Gironcoli, S. Fabris, G. Fratesi, R. Gebauer, U. Gerstmann, C. Gougoussis, A. Kokalj, M. Lazzeri, L. Martin-Samos, N. Marzari, F. Mauri, R. Mazzarello, S. Paolini, A. Pasquarello, L. Paulatto, C. Sbraccia, S. Scandolo, G. Sclauzero, A. P. Seitsonen, A. Smogunov, P. Umari, and R. M. Wentzcovitch, J. Phys.: Condens. Matter **21**, 395502 (2009).
[57] P. Giannozzi, O. Andreussi, T. Brumme, O. Bunau, M. B. Nardelli, M. Calandra, R. Car, C. Cavazzoni, D. Ceresoli, M. Cococcioni, N. Colonna, I. Carnimeo, A. D. Corso, S. de Gironcoli, P. Delugas, R. A. DiStasio, A. Ferretti, A. Floris, G. Fratesi, G. Fugallo, R. Gebauer, U. Gerstmann, F. Giustino, T. Gorni, J. Jia, M. Kawamura, H.-Y. Ko, A. Kokalj, E. Küçükbenli, M. Lazzeri, M. Marsili, N. Marzari, F. Mauri, N. L. Nguyen, H.-V. Nguyen, A. O. de-la Roza, L. Paulatto, S. Poncé, D. Rocca, R. Sabatini, B. Santra, M. Schlipf, A. P. Seitsonen, A. Smogunov, I. Timrov, T. Thonhauser, P. Umari, N. Vast, X. Wu, and S. Baroni, J. Phys.: Condens. Matter **29**, 465901 (2017).
[58] M. Lazzeri and S. de Gironcoli, Phys. Rev. Lett. **81**, 2096 (1998).
[59] L. Paulatto, F. Mauri, and M. Lazzeri, Phys. Rev. B **87**, 214303 (2013).
[60] G. Fugallo, A. Cepellotti, L. Paulatto, M. Lazzeri, N. Marzari, and F. Mauri, Nano Lett. **14**, 6109 (2014).
[61] A. Cepellotti, G. Fugallo, L. Paulatto, M. Lazzeri, F. Mauri, and N. Marzari, Nat. Commun. **6**, 6400 (2015).
[62] L. Paulatto, I. Errea, M. Calandra, and F. Mauri, Phys. Rev. B **91**, 054304 (2015).